Journal of Glaciology

Article

Cite this article: Mahagaonkar A, Moholdt G, Glaude Q, Schuler TV (2024). Supraglacial lake evolution and its drivers in Dronning Maud Land, East Antarctica. *Journal of Glaciology* **70**, e49, 1–15. https://doi.org/10.1017/jog.2024.66

Received: 2 February 2024
Revised: 23 July 2024
Accepted: 11 August 2024

Keywords:
Antarctic glaciology; ice/atmosphere interactions; ice shelves; melt – surface; remote sensing

Corresponding author:
Anirudha Mahagaonkar;
Email: anirudha.vm@gmail.com

cambridge.org/jog

Supraglacial lake evolution and its drivers in Dronning Maud Land, East Antarctica

Anirudha Mahagaonkar[1,2], Geir Moholdt[1], Quentin Glaude[3,4] and Thomas Vikhamar Schuler[2]

[1]Glaciology and Geology Section, Norwegian Polar Institute, Tromsø, Norway; [2]Department of Geosciences, University of Oslo, Oslo, Norway; [3]Laboratory of Climatology, University of Liège, Liège, Belgium and [4]Centre Spatial de Liège, Laboratory of Signal Processing, University of Liège, Liège, Belgium

Abstract

Supraglacial lakes on Antarctic ice shelves can have far-reaching implications for ice-sheet stability, highlighting the need to understand their dynamics, controls and role in the ice-sheet mass budget. We combine a detailed satellite-based record of seasonal lake evolution in Dronning Maud Land with a high-resolution simulation from the regional climate model Modèle Atmosphérique Régional to identify drivers of lake variability between 2014 and 2021. Correlations between summer lake extents and climate parameters reveal complex relationships that vary both in space and time. Shortwave radiation contributes positively to the energy budget during summer melt seasons, but summers with enhanced longwave radiation are more prone to surface melting and ponding, which is further enhanced by advected heat from summer precipitation. In contrast, previous winter precipitation has a negative effect on summer lake extents, presumably by increasing albedo and pore space, delaying the accumulation of meltwater. Downslope katabatic or föhn winds promote ponding around the grounding zones of some ice shelves. At a larger scale, we find that summers during periods of negative southern annular mode are associated with increased ponding in Dronning Maud Land. The high variability in seasonal lake extents indicates that these ice shelves are highly sensitive to future warming or intensified extreme events.

1. Introduction

Ice shelves are floating extensions of the land-based Antarctic Ice Sheet and play a critical role for their stability. As climate gets warmer, ice shelves are becoming increasingly vulnerable to melting from below and above, which can accelerate the ice discharge from the grounded ice sheet into the ocean and contribute to sea-level rise (Dupont and Alley, 2005; Pritchard and others, 2009; Gagliardini and others, 2010; Rignot and others, 2013; Fürst and others, 2016; Agosta and others, 2019; Datta and others, 2019). Although Antarctic meltwater runoff is currently a minor component in the mass balance of the ice sheet (Bell and others, 2018; van Wessem and others, 2018), there is substantial surface melting in many coastal regions (Trusel and others, 2012; Johnson and others, 2022) and also widespread presence of supraglacial lakes and streams (Kingslake and others, 2017; Stokes and others, 2019; Arthur and others, 2022). In Antarctica, most of the meltwater produced due to melting of snow percolates and refreezes in the underlying firn layer, whereas the excess water ponds in topographical depressions as slush (Dell and others, 2022, 2024), firn aquifers (Buth and others, 2022) and/or supraglacial lakes (Stokes and others, 2019). Accumulation of meltwater in supraglacial lakes may lead to flexure of ice shelves (Banwell and others, 2013, 2019, 2024; Banwell and MacAyeal, 2015; Glaude and others, 2020), hydro-fracture (Rott and others, 1996; Scambos and others, 2000) and collapse (Scambos and others, 2009; Banwell and others, 2013), thereby increasing upstream ice velocity due to decreased buttressing (Rignot, 2004; Glasser and others, 2011). In rare cases, meltwater can drain englacially/subglacially (e.g. Tuckett and others, 2019; Dunmire and others, 2020; Spergel and others, 2021; Warner and others, 2021; Banwell and others, 2024) potentially opening up crevasses and fractures (e.g. Banwell and others, 2013). These consequences make supraglacial lakes a key component of ice-shelf stability and highlight the need to monitor their development in the context of future climate warming (Gilbert and Kittel, 2021). Pervasive supraglacial lakes have been widely reported in the Antarctic Peninsula (Scambos and others, 2000; Leeson and others, 2020; Banwell and others, 2021), but it is only recently that the occurrence and evolution of supraglacial lakes around the fringes of East Antarctica have caught the attention of the scientific community (e.g. Kingslake and others, 2017; Stokes and others, 2019; Dirscherl and others, 2021; Arthur and others, 2022).

Stokes and others (2019) identified widespread presence of supraglacial lakes along the coastal margin of East Antarctica. They form active hydrological networks comprising lateral streams and lakes that can transport meltwater onto and across ice shelves (Kingslake and others, 2017; Dell and others, 2020). Supraglacial lakes in East Antarctica have been studied at various scales and for different periods (e.g. Langley and others, 2016; Arthur and others, 2020, 2022; Dell and others, 2020, 2022; Dirscherl and others, 2021; Tuckett and others, 2021; Saunderson and others, 2022), but few studies go beyond linking lake evolution with global climate reanalysis data (e.g. Langley and others, 2016; Dirscherl and others, 2021; Arthur

and others, 2022). While these global climate products are well suited to represent large-scale atmospheric phenomena, they may not well-represent regional to local-scale processes that arise from complex surface topography. Therefore, the use of a high-resolution regional climate model can be helpful to identify drivers of lake extent variability, especially in the absence of in situ data.

Here, we adopt a region-focused approach using observational records from optical satellite data in combination with a high-resolution regional climate model to investigate the role of local kilometer-scale phenomena in driving the evolution of supraglacial lakes in Dronning Maud Land during 2014–21. We use a band-reflectance thresholding method (Moussavi and others, 2020) to perform a regional and multi-seasonal mapping of lake extents, including their depths derived from a physically based radiative transfer model (Pope and others, 2016). For climatic assessments, we perform a simulation with the regional climate model, Modèle Atmosphérique Régional (MAR; Gallée and Schayes, 1994) at a high spatial resolution of 5 km that allows us to better resolve local topography. Additionally, we also use climate reanalysis datasets (mainly for comparison) and climate indices for assessing large-scale drivers. We analyze lake–climate relationships through correlations between various climatic variables and lake extents over different years. Findings from this study allow us to improve our understanding of different topographically driven climatic controls on supraglacial lakes in Dronning Maud Land, which may have implications for future ice-shelf stability in the region.

2. Study area: Dronning Maud Land

Dronning Maud Land (defined here between longitude 20° W and 35° E in East Antarctica; Fig. 1) hosts a series of ice shelves and embayments separated by many ice rises and ice-sheet promontories (Goel and others, 2020). The floating shelves are fed by a number of ice streams, the most prominent being Plogbreen and Veststraumen in the west, Jutulstraumen, Potsdam Glacier and Tussebreen in the center and West and East Ragnhild glaciers in the east. With a coastline of ~2600 km and a narrow continental shelf, the ice shelves are exposed to strong ocean and sea-ice interactions. The rugged ice-sheet topography gives rise to complex patterns of snow erosion and accumulation, including extensive blue ice areas (Fig. 1). Within the region, exposed blue ice is concentrated mostly to the south and southeast of the ice shelves, typically on the slopes above the grounding lines. These blue ice areas are formed due to scouring by sustained downslope winds blowing from the ice-sheet interior (Das and others, 2013). With lower surface albedo, these areas experience enhanced shortwave radiation absorption thereby promoting surface melting and subsequent meltwater ponding. Satellite-radar backscatter time series have been used to estimate surface melt rates over the entire continent, and indicate that the highest surface melt rates in Dronning Maud Land are found on the Roi Baudouin Ice Shelf, at ~120 mm w.e. a^{-1} followed by Nivlisen ~80 mm w.e. a^{-1} and Riiser Larsen ~70 mm w.e. a^{-1} (Trusel and others, 2013). Using satellite observations, various studies have identified and mapped supraglacial lakes on Riiser Larsen, Nivlisen and Roi Baudouin ice shelves in Dronning Maud Land (Kingslake and others, 2015; Stokes and others, 2019; Dell and others, 2020, 2022; Moussavi and others, 2020; Dirscherl and others, 2021; Arthur and others, 2022) and over the floating tongue of Langhovde (Langley and others, 2016) which is just east of the study area. Additionally, several small-sized proglacial and epishelf lakes are found around the Schirmacher Oasis (Phartiyal and others, 2011) due to the albedo-lowering feedback from rock outcrops (Winther and others, 1996; Kingslake and others, 2017; Stokes and others, 2019).

3. Data and methods

To identify all regions with considerable supraglacial lake occurrences within Dronning Maud Land, we manually assessed ~120 Landsat 8 scenes captured in January 2017 and January 2021, representing the peak melting periods of these 2 years. The chosen scenes covered the entire swath of the study area from west to east. Careful visual inspection of these scenes was carried out to identify regions with possible lake occurrences (demarcated in Fig. 1). We identified five ice shelves with significant lake ponding: Riiser Larsen, Fimbulisen, Nivlisen, Muninisen and Roi Baudouin (Fig. 1). Further assessments of lake evolution (Section 3.1) were restricted to scenes covering these regions to save computation time, but to include areas with significant

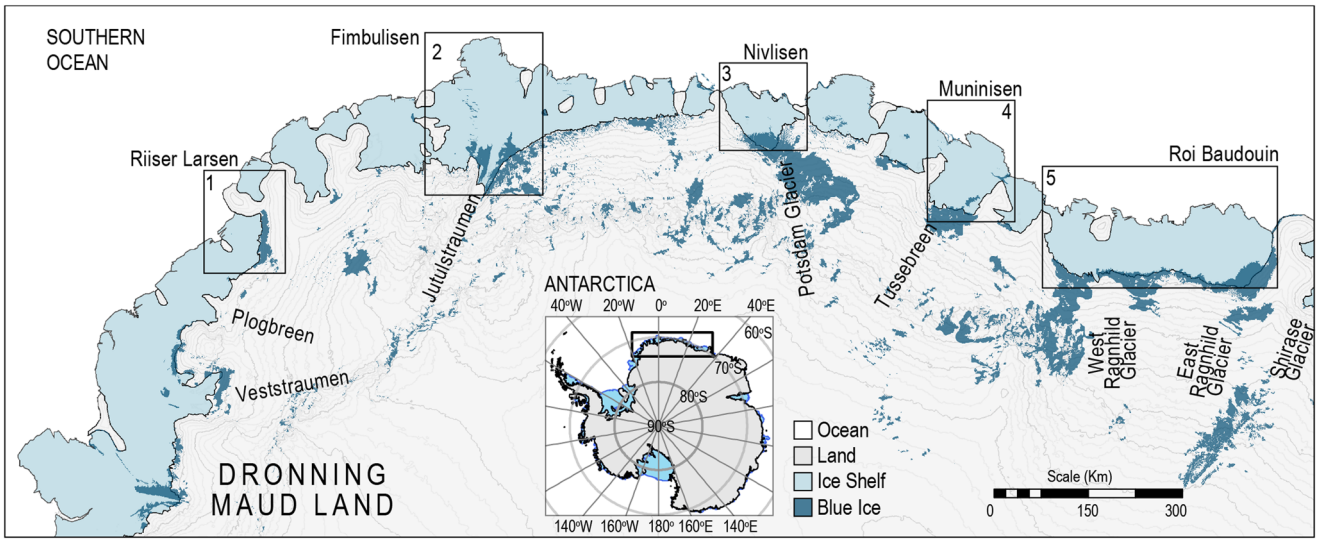

Figure 1. Map of Dronning Maud Land highlighting the different ice shelves on which supraglacial lakes are identified in the study: (1) Riiser Larsen, (2) Fimbulisen, (3) Nivlisen, (4) Muninisen and (5) Roi Baudouin. The small inset map shows the location of Dronning Maud Land within Antarctica. In the background are 100 m contours representing the overall surface topography, generated using the REMA 100 m product (Howat and others, 2019). The dark blue colored areas show the exposed blue ice areas as mapped from satellite imagery (Hui and others, 2014). Antarctic outlines were sourced from SCAR's Antarctic Digital Database (ADD) through Quantarctica (Matsuoka and others, 2021).

https://doi.org/10.1017/jog.2024.66 Published online by Cambridge University Press

sized lakes. Climatic evaluations were performed using different datasets as further described in Section 3.2. The potential albedo-lowering impact of rock outcrops was not considered because the rock outcrops are 80–120 km away from the identified lake regions, except for the mentioned Schirmacher Oasis near the Nivlisen Ice Shelf.

3.1. Supraglacial lake extent, depth and volume

For the semi-automated lake mapping, all available optical scenes from Landsat 8 (sensors – Operational Land Imager and Thermal Infrared Sensor) and Sentinel-2 (sensor – Multispectral Instrument) acquired between 1 November and 31 March during the period 2014–21 were manually inspected to exclude scenes with clouds covering potential lake regions. Manual inspection was done to enable inclusion of cloudy scenes with clear windows over areas of interest. Of the ~2500 scenes inspected, ~1100 were suitable and used for mapping (listed in Supplement 2). Lake mapping was performed following recommendations of Moussavi and others (2020), briefly summarized here. For Landsat 8 scenes, we used bands representing blue, green, red, shortwave infrared and thermal infrared, whereas for Sentinel-2 we used blue, green, red and the two available shortwave infrared bands. After pre-processing the data to represent top of atmosphere reflectance, we generated snow masks, cloud masks and rock/sea-water masks by applying various thresholds to different band combinations and indices. These masks were used to eliminate potentially misclassified water pixels from the water mask that was generated by applying thresholds to the normalized difference water index adopted for water on snow and ice ($NDWI_{ice}$). A threshold of 0.25 was used for $NDWI_{ice}$ instead of 0.19 suggested by Moussavi and others (2020) to avoid inclusion of slush and shallow ponds due to their spectral overlap with clouds and shadows over blue ice (further explained in Section S1.3). Manual inspection was carried out before finalization to eliminate potential remaining large, misclassified pixel groups (an example is presented in Fig. S5). Using the final lake masks, recurrence plots (Fig. 2) were constructed for all lake regions by overlaying lake extents from every year.

Lake depths were estimated for each water pixel using a physically based radiative transfer model (Pope and others, 2016; Moussavi and others, 2020), which assumes that the attenuation of light in a water column is a function of the length of the column, that is, the water depth of the lake. Lake volumes were calculated by multiplying the estimated depth of each pixel by its surface area and summing them together. Lake areas and lake depths from Landsat 8 and Sentinel-2 were cross-validated using four pairs of Landsat 8 and Sentinel-2 scenes that were captured on the same day, at around similar times (listed in Table S1). The two datasets showed strong consistency with a correlation $r = 0.96$ for lake area and $r = 0.89$ for lake depth (RMSE = 0.21 m, Fig. S2). All grids of lake extent and depth were reprojected to Antarctic Polar Stereographic – EPSG:3031 projection and resampled to a fixed grid of 30 m spatial resolution for consistency. A detailed step-by-step procedure for lake mapping, depth and volume estimation is provided in Section S1 and Figure S1 of the Supplementary materials. As a part of the analyses, we also quantified different error sources and quantified uncertainty, briefly summarized here with more details in Supplementary Section S1.6. Various error sources, primarily cloud shadows, blue ice, nunataks and crevassed areas, were

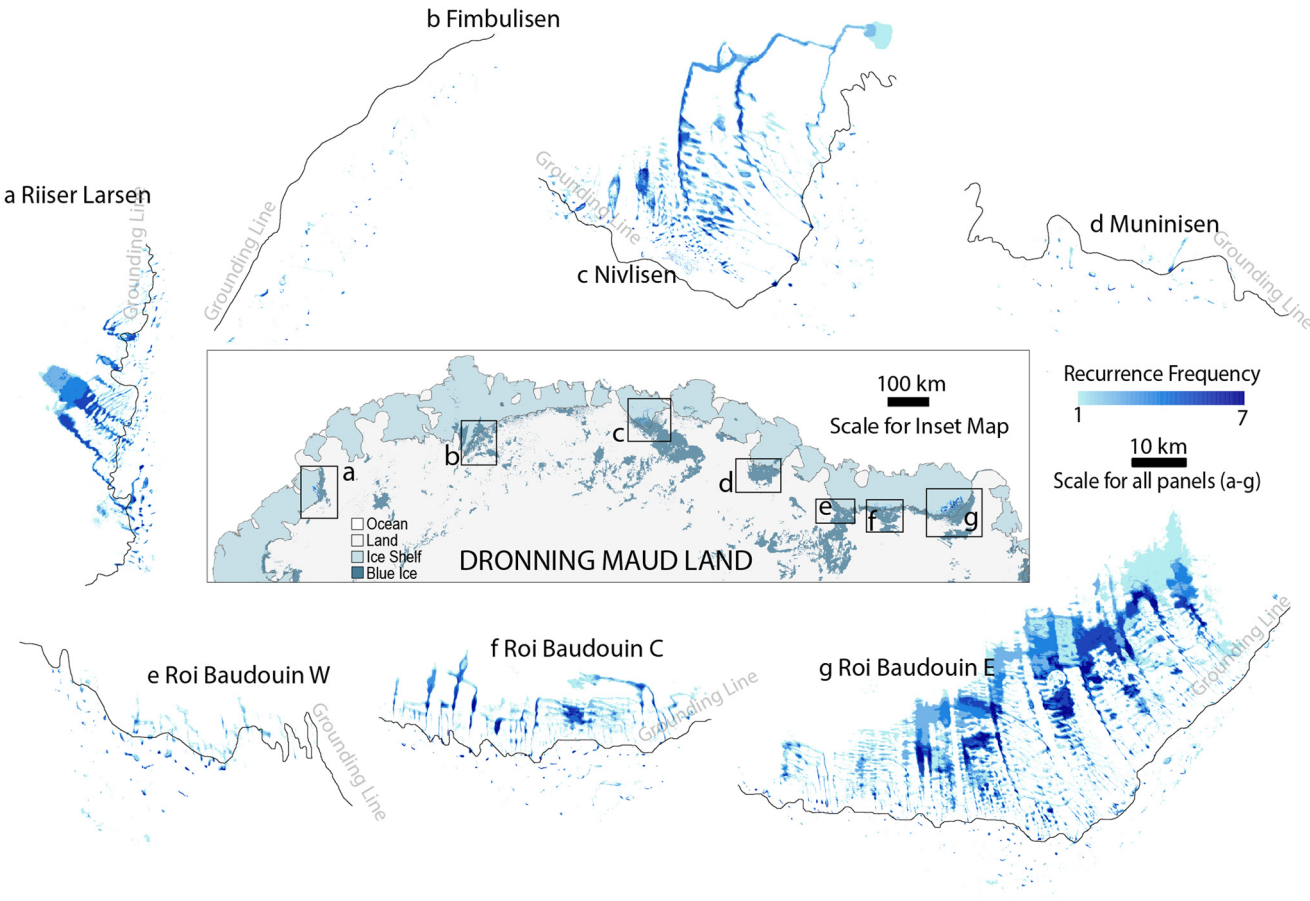

Figure 2. Spatial distribution and recurrence of supraglacial lakes on the five ice shelves in Dronning Maud Land. The blue color scale indicates the number of times a particular pixel was classified as water between the 2014/15 and 2020/21 melt seasons. Value 1 indicates water only in one of the seven seasons of observation, whereas seven indicates water in every melt season.

https://doi.org/10.1017/jog.2024.66 Published online by Cambridge University Press

identified through manual inspection. Large groups of such misclassified pixels were manually eliminated (e.g. Fig. S5), whereas it was not feasible to remove smaller groups. Difference in total lake area from cross-validation of manually digitized lakes and automatically mapped outlines (Fig. S3) was found to be ~0.5–0.7%; based on this, we adopt a conservative uncertainty estimate of 1% of lake area. Given the close relationship between lake areas and volumes (Liang and others, 2012; Trusel and others, 2012), we applied the same error estimate for volumes but upscaled it with an empirical error for lake depth (0.21 m; which is the RMSE from Fig. S2). To assess the uncertainty in capturing the maximum lake extents, which are used in the correlation analysis (Section 3.2.5), the timing of available satellite data relative to the peak melt season was considered, with stages conceptualized to represent different phases of meltwater ponding. Five scenarios for data availability were outlined, ranging from worst case (95% uncertainty) to best case (5% uncertainty). The corresponding relative uncertainties were assigned to the maximum area (or volume) estimates for each scenario (Table S2), in addition to the 1% assigned above.

3.2. Climate data and relationships with supraglacial lakes

To identify climatic factors driving lake changes, we performed a correlation analysis between summer lake extents and various climatic variables (Section 3.2.5). Selected climatic variables and their characteristics are summarized in Table 1. Energy fluxes are defined as positive when directed toward the surface (energy gain) and as negative away from the surface (energy loss). To investigate large-scale atmospheric variability, we assessed the southern annular mode (SAM) and dipole mode index (DMI).

3.2.1. ER5 and ERA5-Land climate reanalysis

We used daily continental and regional temperature estimates from ERA5 (Copernicus Climate Change Service (C3S), 2017; Hersbach and others, 2020) and ERA5-Land (Muñoz-Sabater and others, 2021) to check for consistency and for comparison with other studies that have used these data (e.g. Dirscherl and others, 2021). ERA5 is the fifth-generation product of European Centre for Medium-Range Weather Forecasts (ECMWF) atmospheric reanalysis of global climate, with data available from 1940 onward. It replaces ERA-Interim (Dee and others, 2011) and has a grid resolution of 0.25° (~31 km) assimilating large-scale observational data from satellites, ocean buoys and ground stations using advanced numerical models to provide hourly simulations of several climate variables. ERA5-Land, an extension of ERA5, is specifically focused on land-surface parameters providing hourly climate data at 0.1° (~11 km) grid resolution, a significant upgrade over ERA5 (0.25° or ~31 km) and ERA-Interim (0.75° or ~83 km). Both global reanalysis products are widely used in studies concerning Antarctic weather, climate and supraglacial lake evolution.

3.2.2. MAR regional climate model

We also applied daily data from the MAR, a regional climate model extensively used in polar research, in this study. We used MARv3.12 (Lambin and others, 2023), which includes parametrizations based on the methods of Kittel and others (2021). The model has undergone thorough evaluation against near-surface data from automatic weather stations (Datta and others, 2018; Kittel and others, 2021; Mottram and others, 2021) including radiative fluxes (Hofer and others, 2021; Kittel and others, 2021) over the Antarctic Ice Sheet. Our configuration of MAR was at a horizontal resolution of 5 km over Dronning Maud Land, and as lateral boundary conditions we used 6 hourly ERA5 reanalysis data from the period 2014 to 2021, following an initial spin-up phase from 2010 to 2013 for atmospheric conditioning. This high spatial resolution enables capturing of local-scale processes which can potentially influence surface melting in the region, directly or indirectly.

MAR is based on the hydrostatic approximation of primitive equations as detailed by Gallée and Schayes (1994). It includes a microphysics module that manages five types of water entities (Gallée, 1995). The model also integrates a radiative transfer scheme based on the ECMWF ERA-40 reanalysis (Morcrette, 2002) and utilizes the Soil Ice Snow Vegetation Atmosphere Transfer module to simulate interactions between the atmosphere and the surface (De Ridder and Gallée, 1998). MAR includes the CROCUS snow model (Brun and others, 1992), representing the snow metamorphism across multiple layers. Additionally, MAR calculates dynamic surface albedo, accounting for changing snow properties and cloud coverage (Tedesco and others, 2016), and integrates comprehensive models for atmospheric and sea surface conditions. The model's snowpack is discretized in 30

Table 1. Climatic variables used in the study and their characteristics

Category	Variable	Averaging: summer (DJ) average or annual cumulative	Climate dataset	Resolution/ scale
Temperature	*ERA5* Surface Temperature	Summer (DJ) average	ERA5	0.25° (~31 km)
	ERA5-Land Surface Temperature	Summer (DJ) average	ERA5-Land	0.1° (~11 km)
	MAR Surface Temperature	Summer (DJ) average	MAR	5 km
	Maximum Surface Temperature	Summer (DJ) maximum	MAR	5 km
Precipitation	Rainfall	Summer (DJ) average	MAR	5 km
	Snowfall	Summer (DJ) average	MAR	5 km
	Seasonal Precipitation (Rainfall + Snowfall)	Summer (DJ) average	MAR	5 km
	Annual Precipitation (Rainfall + Snowfall)	Annual cumulative	MAR	5 km
Energy fluxes	Energy available for heating/melt (= sum of all individual energy fluxes)	Summer (DJ) average	MAR	5 km
	Net Shortwave Radiation	Summer (DJ) average	MAR	5 km
	Net Longwave Radiation	Summer (DJ) average	MAR	5 km
	Sensible Heat Flux	Summer (DJ) average	MAR	5 km
	Latent Heat Flux	Summer (DJ) average	MAR	5 km
Winds	Wind Speed (10 m)	Summer (DJ) average	MAR	5 km
	Föhn Days	Summer (DJ) average	Estimated using MAR	5 km
	Wind Speed during föhn days	Summer (DJ) average	Estimated using MAR	5 km
	Katabatic Days	Summer (DJ) average	Estimated using MAR	5 km
	Wind Speed during Katabatic Days	Summer (DJ) average	Estimated using MAR	5 km
Climate indices	SAM	Summer (DJ) average	–	>100 km
	DMI	Summer (DJ) average	–	>100 km

DJ, December, January.

https://doi.org/10.1017/jog.2024.66 Published online by Cambridge University Press

layers, representing the uppermost 20 m of the ice sheet, at varying vertical resolutions (the upper layers being thinner).

3.2.3. Föhn days and katabatic days

To identify topographically governed wind effects, such as föhn and katabatic flows, we estimate föhn days and katabatic days corresponding to the number of days with respective event occurrences using daily MAR data. Föhn winds are warm and dry winds that occur on leeward (downslope) sides of mountains (Cape and others, 2015) and are characterized by prolonged increases in surface temperature, wind speed and decreases in humidity. Based on a previous study on the Antarctic Peninsula (Datta and others, 2019), we define the onset of föhn activity when temperature increases by ⩾1°C, wind speed increases by ⩾3.5 m s^{-1} and relative humidity decreases by ⩾5%, relative to the conditions preceding the föhn initiation. When one of these conditions fails, the föhn event ceases. Each time the föhn conditions are fulfilled, it accounts for a föhn day irrespective of the duration of the föhn event.

Katabatic winds are downslope, cold and dry winds flowing from the interior of the ice sheet toward the coast driven by gradients in air pressure and density (Parish and Bromwich, 1987). Due to radiative cooling of air parcels (especially during austral winter and nights of austral summer), the air becomes denser and follows gravitational pull by flowing downhill, causing an increase in wind speed. As this cold air descends, it causes vertical mixing and undergoes adiabatic compression, leading to a rise in temperature. We identify katabatic activity in the region using the wind direction and surface topography (represented by aspect). First, we use the surface elevation model used in MAR (Bedmap2 DEM; Fretwell and others, 2013) to calculate the aspect orientation. The elevation model was smoothened using an averaging 3 × 3 window to minimize artifacts and eliminate minor topographic variations which do not have an impact on the wind direction. Any air flow aligned with the aspect (i.e. following the surface topography) is defined as katabatic. However, to account for minor deviations in the wind direction and the effect of the Coriolis force (Davis and Mcnider, 1997), which causes winds to deflect more toward the left in the Southern Hemisphere, we defined an aspect range (from aspect −30° to aspect +15°, where ±15° accounts for minor wind deviations and an additional −15° allows for deviation due to Coriolis). Each time the katabatic condition is fulfilled, it accounts for one katabatic day.

3.2.4. SAM and DMI climate indices

To investigate the role of large-scale climate patterns in meltwater ponding (e.g. Dirscherl and others, 2021), we compared our mapped lake extents against the Marshall SAM (Marshall, 2003) and the DMI. Using pressure differences from six ground stations across the Southern Hemisphere, SAM represents the northward and southward movement of westerlies in the Southern Hemisphere highlighting atmospheric variability from month to month. This variability has an impact on regional climate in Antarctica, including surface temperature, and oceanic and atmospheric circulation (Marshall, 2003). The positive phase of SAM corresponds to stronger westerlies in the mid-latitudes and contracted polar vortex, whereas the negative phase represents weaker westerlies and expanded polar vortex. The Indian Ocean dipole, represented through the DMI, corresponds to atmospheric pressure differences between the eastern Indian Ocean (near Australia) and western Indian Ocean (near Africa). The positive phase of the DMI relates to warmer sea surface temperature and lower atmospheric pressure in the western Indian Ocean and cooler sea surface temperature and higher atmospheric pressure in the East Indian Ocean, and vice versa in the negative phase.

3.2.5. Correlation analysis

For each lake region, we calculated Pearson's correlation coefficient, r (range: −1 to +1) between seasonal maximum lake areas and chosen climatic variables for each austral summer from 2014 to 2021 ($n = 7$). The seasonal maximum lake area refers to the peak extent of lakes within each melt season, determined for each season by selecting a single output from the mapped time series in this study. Since almost all ponding occurs during the summer months December and January, we restrict the averaging of climate variables to this 2 month period except for annual precipitation (cumulative from the preceding January to December). To identify model gridpoints to be used in the assessment for each region, we drew polygons around the lake areas of interest for each region (Fig. S6; top) and identified intersecting MAR/ERA5/ERA5-Land gridpoints (Fig. S6; panels 1–5). These polygons were drawn based on the regional maximum extent of lakes seen through recurrence plots (Fig. 2) and are meant to represent the areas where meltwater is generally produced, that is, close to the grounding zones. Data from these intersecting gridpoints were then used to calculate regional averages of each climate variable for each year. For SAM and DMI, correlations were drawn with respect to their average summer (DJ) values. To assess the influence of larger-scale atmospheric/oceanic circulation patterns on near-surface temperatures, we also calculated correlations between climate indices (both summer and annual) and continental temperatures. These temperature values were averaged over all ERA5 gridpoints on land in Antarctica.

4. Results

4.1. Spatial distribution of supraglacial lakes

In most years, supraglacial lakes form on (or close to) five ice shelves in Dronning Maud Land (Fig. 2) – Riiser Larsen, Fimbulisen, Nivlisen, Muninisen and Roi Baudouin. Among these, Roi Baudouin has the most extensive ponding, spread over three distinct parts of the ice shelf (Roi Baudouin West, Roi Baudouin Center and Roi Baudouin East, Figs 2e–g). Despite comparable environmental settings, no significant meltwater ponding is observed on nearby ice shelves such as Quarisen, Ekströmisen, Jelbartisen, Vigridisen, Vidisen, Lazarevisen, Huginisen or Jotneisen.

In the seven identified regions, supraglacial lakes are primarily distributed around the grounding zones, extending laterally over parts of the ice shelves (Fig. 2). On average, ∼10–15% of the total lake area lies on the grounded part of the ice sheet, while the rest extends over the floating ice shelves. Supraglacial lakes in the seven regions are visible as circular ponds and lakes of different sizes, extending up to 30 km^2 (even larger when coalesced), and as streams with channelized flow of meltwater. Lake densities are highest on Roi Baudouin East and lowest on Muninisen. Nivlisen and Riiser Larsen also have relatively high densities of supraglacial lakes, particularly during years with high ponding (2016/17 and 2019/20). Lake depths are generally similar across all the regions, with an overall seasonal mean lake depth of 1.31 ± 0.27 m. Lakes on Nivlisen have the highest overall mean depth at 1.94 ± 0.30 m, whereas the deepest water body is found on Roi Baudouin East with a lake depth of 3.46 ± 0.29 m, followed by a 3.41 ± 0.30 m deep feature on Riiser Larsen. Both of these observations are from the peak ponding periods, that is, mid-January.

Considering the topographical distribution, quantitatively assessed using the reference elevation model of Antarctica (REMA) at 100 m resolution (Howat and others, 2019), most lakes are present at elevations below 100 m (Fig. S14) with low surface slopes, while the highest lake observed is at 409 m above sea level in the Roi Baudouin East region. In general, this distribution varies between years with high ponding (e.g. 2016/17;

https://doi.org/10.1017/jog.2024.66 Published online by Cambridge University Press

Fig. S14c) and low ponding (e.g. 2020/21; Fig. S14b). During low-ponding years, visible advection of meltwater is limited to only a few kilometers below the grounding zone (e.g. Fig. S8). Transportation of meltwater occurs primarily through elongated streams that originate near the grounding zone and end up in various circular lakes downstream over the ice shelf. From the recurrence plots (Fig. 2), it is evident that supraglacial lakes form a network of channels and usually flow through the same channels year after year. Riiser Larsen, Nivlisen and Roi Baudouin ice shelves have well-established networks that transport meltwater over larger distances, whereas lateral surface meltwater transport is minimal on Fimbulisen and Muninisen.

4.2. Temporal variations of supraglacial lakes

4.2.1. Seasonal evolution

In all regions, meltwater ponding is first observed close to the grounding zone between mid-November and early-December. However, ponding area is minimal during this initial period (e.g. Fig. 3a; red arrows pointing at early ponds near Nivlisen in 2018/19 melt season). Meltwater accumulation increases from mid-December onwards, mainly in smaller depressions over the areas close to the grounding zone (Figs 3b–d). As these depressions start to overflow, advection of meltwater occurs through streams across the grounding zones over to the flatter ice shelves (Fig. S7). A substantial increase in ponding area is recorded between early and mid-January (Figs 3e–g), and shortly after we capture the peaks of meltwater ponding, that is, when areas and volumes of lakes are at the maximum (mid-January to end of January; Figs 3h, i). During this period, significant advection of meltwater occurs across several ice shelves (e.g. Fig. 3 and Supplementary Animation 1). Thereafter, as air temperatures drop (Fig. S4a), lakes begin to freeze (Figs 3j–l) with thin layers of ice appearing on lake surfaces (see the more detailed Fig. 6g), continuing until end of March when almost no surface meltwater is present (Fig. 6h). The evolution of lakes during high-ponding years and low-ponding years is very different. Ponding and advection of water is minimal during low-ponding years (e.g. Fig. S8 – 2020/21 melt season over Nivlisen), whereas during high-ponding years (e.g. Fig. 3 – 2018/19 melt season over Nivlisen) ponding is rapid and widespread over the area.

4.2.2. Interannual evolution

All regions exhibit large variability in lake area and volume from year to year (Fig. 4 and Table S3). For Dronning Maud Land as a whole, we see that 2015/16 and 2020/21 are years with little surface ponding (Fig. 4; highlighted with green), whereas 2016/17 and 2019/20 are years where widespread ponding is observed (Fig. 4; highlighted with red). The exception of Roi Baudouin East in 2019/20 is likely attributed to the limited number of cloud-free images, which is reflected in the larger uncertainty bar. In most years, the relative magnitude of surface ponding, high or low, is consistent across all the Dronning Maud Land regions.

The largest annual anomaly of lake area (or volume) in percentage is observed over Muninisen in the 2016/17 melt-season with ~200% larger lake area compared to the mean (Fig. 4b), whereas over Fimbulisen and Riiser Larsen large positive anomalies (~150%) are observed in 2018/19. Nivlisen, on the other hand, has the largest anomaly in 2015/16 with 90% lower area and volume. Interestingly, variations in lake area across the three parts of the Roi Baudouin Ice Shelf are often not in phase. While lakes in Roi Baudouin Center have the largest anomaly in the 2019/20 melt season (~100% higher area and volume), Roi Baudouin West and Roi Baudouin East have the largest anomaly in the 2016/17 melt season (~120% larger in both cases).

4.3. Relationship between lake extents and climate conditions

Correlations between maximum lake extents and various climatic variables show complex patterns (Fig. 5). Significant correlations

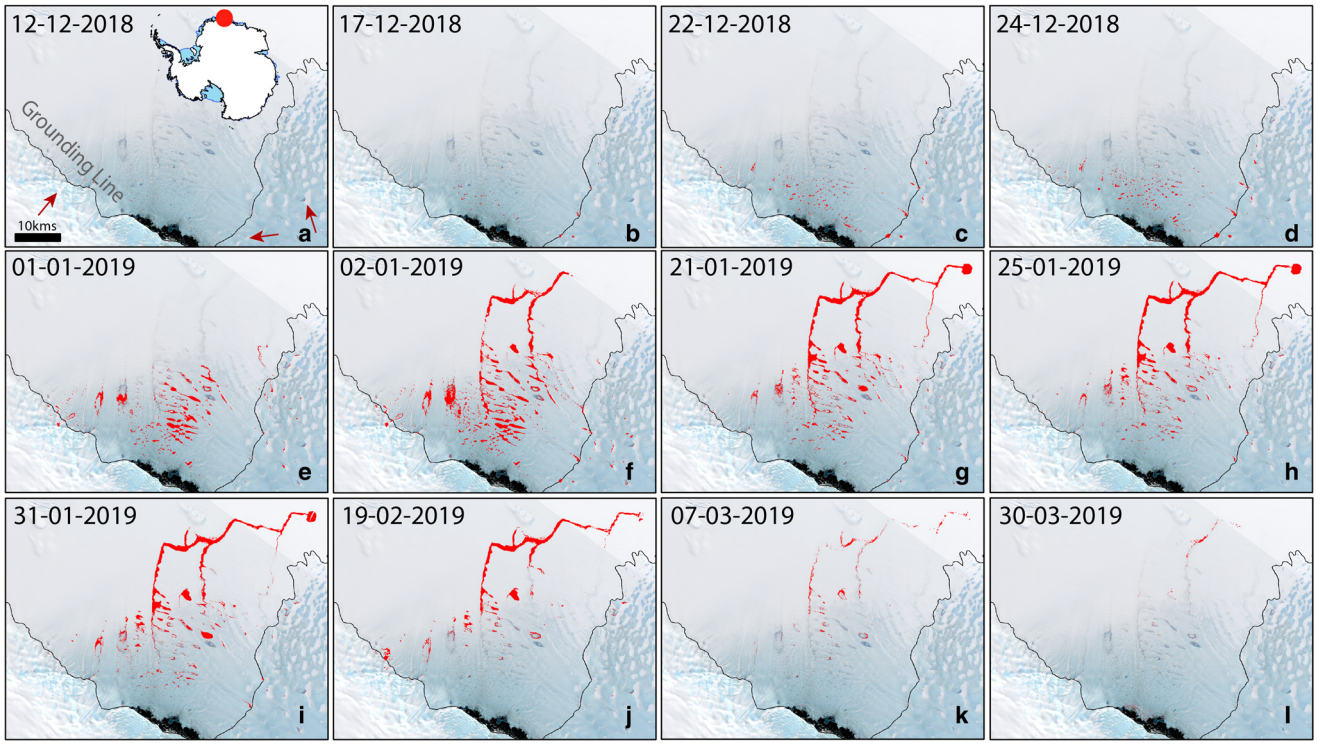

Figure 3. Seasonal evolution of supraglacial lakes over Nivlisen in Dronning Maud Land during a high-ponding year (2018/19) with red color representing the extent of lakes on a specified date. By following each panel in chronological order, the lateral transfer of meltwater can be observed (Supplementary Animation 1). The background image used for representation is a Landsat 8 RGB composite from 3 November 2017 (Source: USGS). Red arrows indicate poorly visible small-sized ponds.

https://doi.org/10.1017/jog.2024.66 Published online by Cambridge University Press

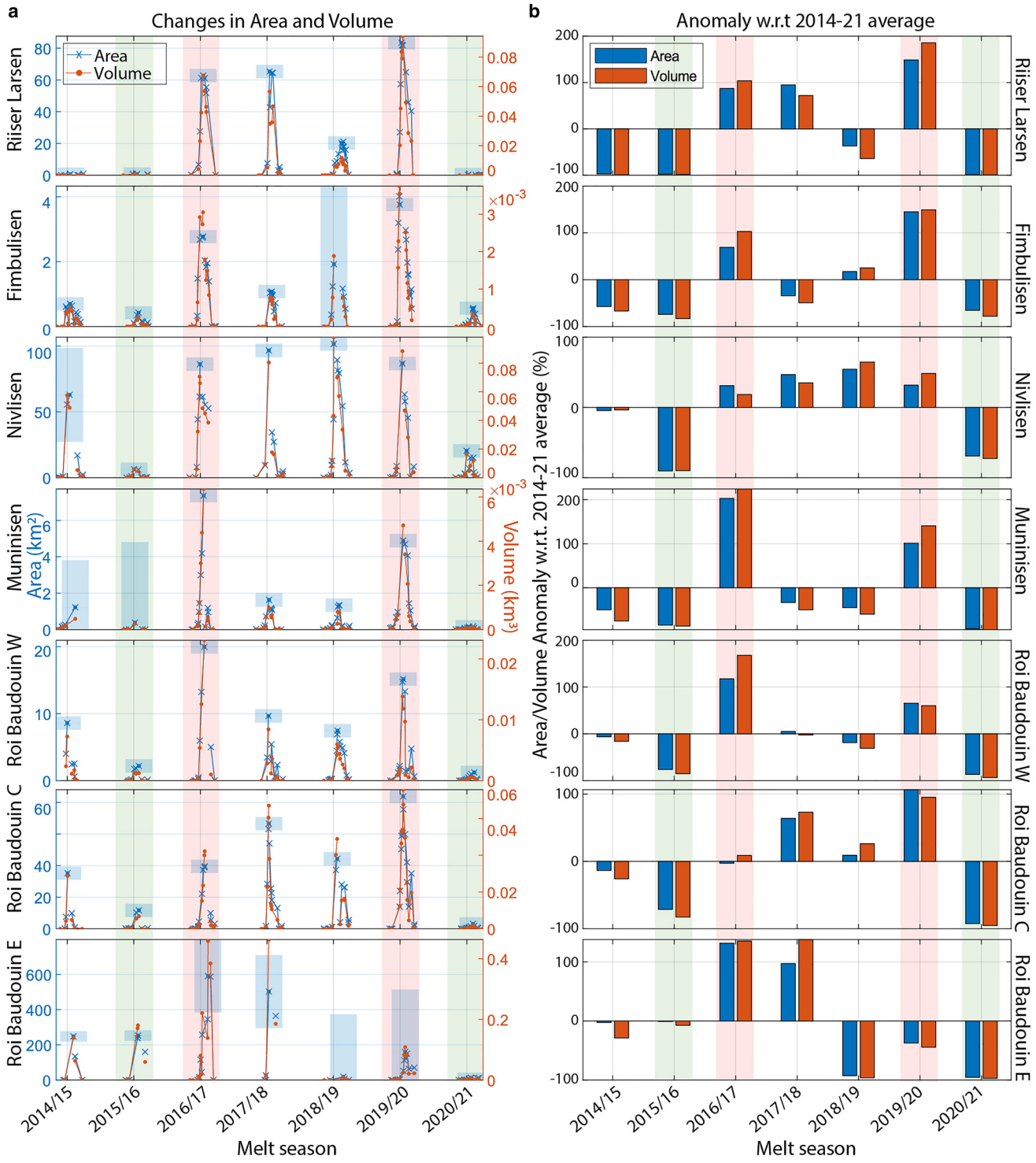

Figure 4. Temporal variation of supraglacial lake area and volume across seven lake regions in Dronning Maud Land. (a) Quantitative changes in lake area and volume between 2014 and 2021 with error bars in blue. Each marker pair denotes the availability of a satellite image, with 'x' indicating area and '.' indicating volume mapped using that image. Subsequent markers are connected to illustrate the temporal evolution of lakes. (b) Anomaly in lake area and volume. Anomaly is determined as the difference between the seasonal maximum lake extent and the 2014–21 average. The 2014–21 average is calculated using maximum lake extents from all the seven melt seasons. In both panels, the red and green shading represent the high- and low-ponding seasons, respectively.

are found for many of the climate variables but not in a consistent way between regions. Near-surface temperature (Fig. 5; MART2M) has the strongest positive correlation for most of the regions, with an average $r = 0.65$. Temperatures from the two global climate reanalysis products, ERA5 and ERA5-Land, have similar correlations (average $r = 0.70$ and 0.71, respectively) as temperature from the regional climate model MAR, despite their coarser spatial resolutions. An exception to the strong temperature relationship is Roi Baudouin East, where lake area shows low correlation with average summer temperatures, but with a strong link to the maximum temperature, which is generally positively correlated with all lake regions. Correlation with summer precipitation (rainfall, snowfall and total precipitation) is mostly positive, whereas the correlation with annual precipitation is more variable on a regional scale, averaging to $r = -0.04$ for all regions combined. The two climate indices representing

https://doi.org/10.1017/jog.2024.66 Published online by Cambridge University Press

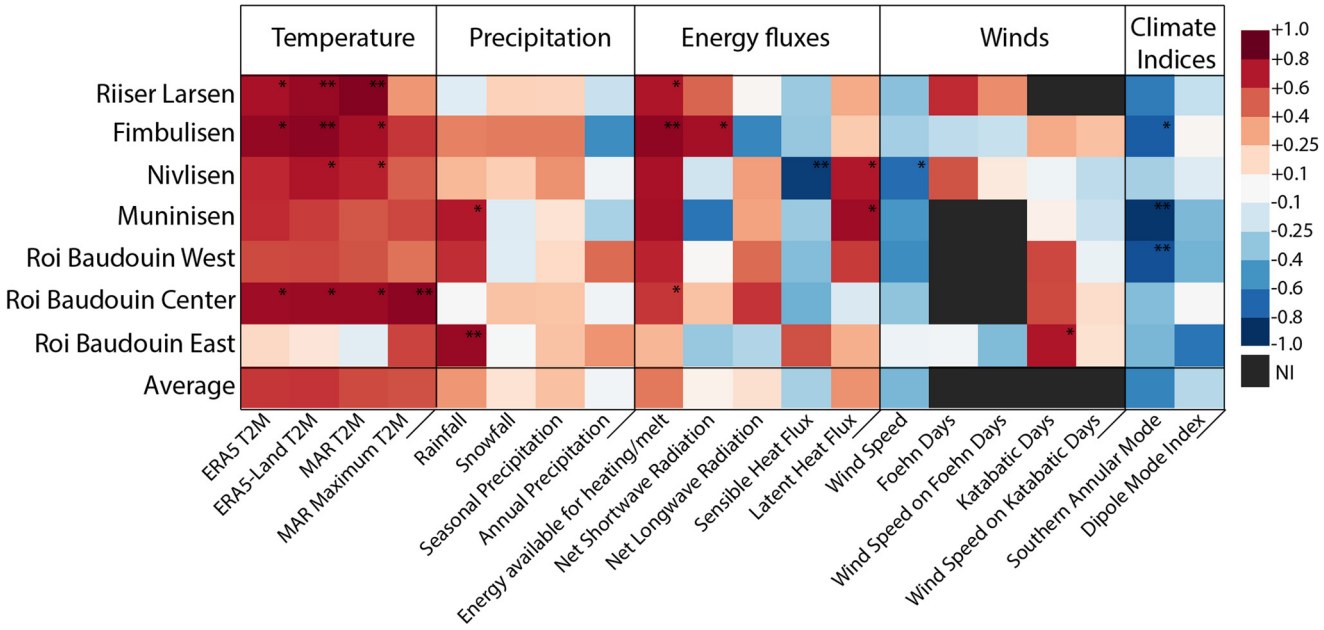

Figure 5. Correlations (*r*) between different lake regions in Dronning Maud Land (rows 1–7) and various climatic variables (columns 1–20). Row 8 shows the average correlation values for rows 1–7. '*' and '**' indicate the statistical significance of correlation (*p*), corresponding to $p < 0.05$ and $p < 0.01$, respectively. Due to the low number of data pairs used for calculating the correlation ($n = 7$ for each lake region), we present and interpret all correlations with $p > 0.05$. Not identified (NI; cells in black) refers to instances where the given events/factors were not identified in our study over a given lake region. This absence is presumably due to lack of topographic features required for föhn winds or the presence of barriers (e.g. nunataks or exposed rock outcrops) that impede the downslope wind flow in case of katabatic winds. Climate model gridpoints from which climate data were extracted for this assessment are shown in Fig. S6 of Supplement 1.

large-scale atmospheric/oceanic patterns, SAM and DMI, are both negatively correlated with seasonal maximum lake extents, but only significantly for SAM. Correlations with energy fluxes are rather heterogeneous, but the energy available for heating/melting (which is the sum of all individual energy fluxes) is positively correlated with seasonal maximum lake extents in all regions. Wind speed shows a consistent negative correlation for all regions, whereas directional wind events quantified as föhn days and katabatic days have strong positive correlations for Riiser Larsen and Roi Baudouin East, respectively. However, averaged wind speeds during these wind events (föhn or katabatic) are less well correlated with lake extents.

5. Discussion

5.1. Distribution and evolution of lakes

Supraglacial lakes are found on five ice shelves in Dronning Maud Land, but with highly variable spatial distribution and extents. For instance, Riiser Larsen, Nivlisen and Roi Baudouin have lakes distributed above the grounding zone as well as on the floating ice shelves, whereas lakes on Fimbulisen and Muninisen are mostly present around the grounding zone. This is indicative of lower surface melting in the latter regions, consistent with independent studies of surface melt extent and duration from satellite scatterometry (Trusel and others, 2012) and passive microwave data (Picard and others, 2007). In general, we cannot rule out the presence of firn aquifers (Buth and others, 2022) and/or subsurface meltwater ponds or streams due to radiative melting underneath the surface (Schlatter, 1972; Brandt and Warren, 1993). Small subsurface hydrological systems were observed by Winther and others (1996) and Liston and others (1999) during their field surveys near Fimbulisen in the 1990s. Such networks can possibly make a delayed contribution to surface ponds through advection or melt-down of the frozen snow/ice lid as summer progresses. More widely, the lake recurrence plots (Fig. 2) show repeated formation of lakes over the same locations, indicating the existence of a locally saturated firn layer with refrozen ice lenses or superimposed ice, which allows for a more rapid progression of ponding in subsequent years. Such ice layers have been observed in areas of intense melting and ponding, for example, on the Larsen C Ice Shelf using ice cores and borehole temperature measurements (Hubbard and others, 2016).

The onset of ponding occurs in mid-November to early-December and lasts until the end of January, in line with the melt durations derived for Dronning Maud Land by Johnson and others (2022) and Trusel and others (2012). During initiation of the ponding season (Figs 3c, d and Figs S8a–c, S9b, c), topographic depressions close to the grounding zone are filled (Fig. S7) implying that most of the meltwater production occurs near the break in surface slope by the grounding zone, which can be attributed to the enhanced interaction with downslope winds and surface scouring (Lenaerts and others, 2017). In this zone, two processes contribute to generation of meltwater: first, the adiabatic warming of descending winds that locally enhance the surface temperature causing snow, firn and ice to melt; and second, the albedo-melt feedback mechanism of exposed blue ice areas (Lenaerts and others, 2017; Bell and others, 2018). Locally enhanced surface temperatures near the grounding zone are clearly visible in model results throughout Dronning Maud Land (Fig. 7a). As the melt season progresses, the meltwater gets laterally transported over the ice shelves by surface streams (Figs 3f–i and Supplementary Animation 1), consistent with findings of Dell and others (2020) for Nivlisen in 2016/17 and Kingslake and others (2017) for several other Antarctic ice shelves. During high-ponding years when feedback mechanisms are expected to be stronger, the transfer of meltwater is higher (e.g. Fig. 3 and Fig. S9), whereas during low-ponding years the transfer is minimal (e.g. Figs S8, S10) due to limited meltwater supply.

Close observation of satellite images reveals different mechanisms through which lakes disappear in the region by the end of the melt season (Fig. 6). Draining into the surrounding snow/firn pack and/or lakes and streams downstream is common and occurs throughout the melt season (Figs 6d, e and 6i, j). As air

https://doi.org/10.1017/jog.2024.66 Published online by Cambridge University Press

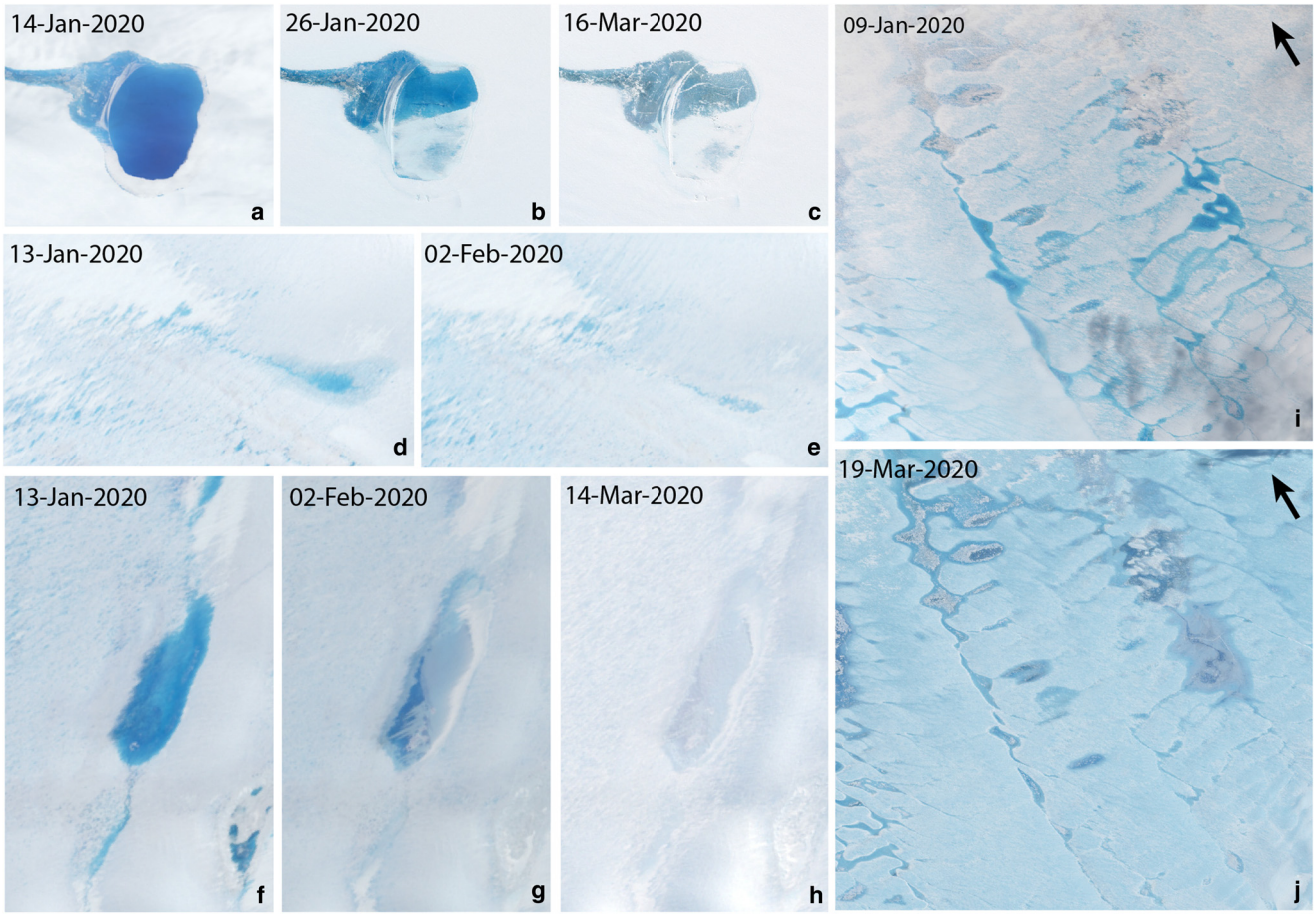

Figure 6. Freeze-up and disappearance of supraglacial lakes seen over different ice shelves in Dronning Maud Land. (a–c) Surficial freezing of deep lakes. The surface ice layer potentially insulates deeper water; (d, e) draining of lakes into surrounding firn/snowpack; (f–h) freezing of shallow lakes potentially to the bottom; (I, j) draining of lakes into lakes downstream/downslope through supraglacial channels. Arrows indicate the flow direction or downstream direction. Images are clipped from Landsat 8 (a, j; Source: USGS) and Sentinel-2 (b, c, d, e, f, g, h, i; Source: Copernicus Open Access Hub) scenes from dates mentioned on respective panels.

temperatures begin to drop, generally after end of January (Fig. S4a), most of the supraglacial lakes begin to freeze, initially forming a thin layer of ice on the surface, then likely freezing to greater depths gradually. The depth to which the supraglacial lakes freeze is unknown. However, based on visual interpretation from Figures 6a–c, f–h, and the simulations by Dunmire and others (2020), we suspect that deeper lakes freeze partially (e.g. Fig. 6c), insulating the water at the bottom (which may freeze later during winter), whereas shallower lakes may freeze completely (e.g. Fig. 6h) by the end of summer (March) or later. As snowfall or snowdrifting occurs, many of these lakes get buried under fresh snow layers, causing further insulation of underlying meltwater (Dunmire and others, 2020) and precluding further observations from space. The modeling experiment by Dunmire and others (2020) demonstrates the sensitivity of surface freezing to snow accumulation, and highlights the possibility for buried non-frozen lakes to exist throughout the cold austral winter.

We found no evidence of lake drainage though crevasses or englacial conduits, but it has been observed previously in Dronning Maud Land by Dunmire and others (2020) in the western part of Roi Baudouin, ~1 km inland from the grounding line. Considering recent observations elsewhere in East Antarctica, for example, on the Amery Ice Shelf (Spergel and others, 2021; Warner and others, 2021) and on the Shackleton Ice Shelf (Arthur and others, 2020), lake drainage through this mechanism could be a more frequent process than previously thought. Runoff over the ice shelf calving fronts (Bell and others, 2018) has not been observed in Dronning Maud Land and there is low probability for this to happen as all identified lake regions are located tens of kilometers from the ice shelf fronts with presumably unsaturated firn areas in between.

5.2. Climate factors driving seasonal meltwater ponding

5.2.1. Temperature

Mean summer temperature is well below freezing for all regions (range: −4.0 to −7.7°C from MAR), with maximum temperatures just ~0°C. For ERA5, ERA5-Land and MAR, there is a consistently strong and positive correlation between mean summer temperature and annual lake extents for all regions ($r = 0.62$–0.93) except for Roi Baudouin East where that is only the case for maximum summer temperature ($r = 0.67$). Correlation with mean summer temperature is expected and in line with findings from other studies (e.g. Langley and others, 2016; Dirscherl and others, 2021; Arthur and others, 2022). The generally high correlation with maximum summer temperature indicates that the lake regions in Dronning Maud Land are sensitive to warm events that can cause rapid peaks in melting with consequent lake expansion. The minimal ponding observed in some years (2015/16 and 2020/21) is a further indication that background summer melt rates are low (or zero), and that maximum lake extents are largely controlled by a limited number of warm events when most (or all) of the melting occurs. Comparing these 2 years with the 2 years of highest observed ponding (2016/17 and 2019/20), regional mean and maximum temperatures were on average 1.8 and 1.0°C warmer during the high-ponding summers.

https://doi.org/10.1017/jog.2024.66 Published online by Cambridge University Press

5.2.2. Precipitation

MAR simulated multiple rainfall events over the study regions, although amounts were minimal (cumulative summer rainfall in Dronning Maud Land on average is 5 mm w.e. a^{-1}). Correlations between rainfall and lake extents are mostly positive, which could be due to the contribution from rainfall itself or the high liquid content of clouds, which increase the longwave radiative flux (Kittel and others, 2022). The correlation mainly relates to the high-ponding summer 2016/17 when all regions except for Riiser Larsen received their highest rainfall of the 7 year record, accounting for ~66% of the total cumulative rainfall on average. On analyzing summer snowfall and summer precipitation (i.e. rainfall + snowfall), correlations are weakly positive for both variables in most regions. A generally positive correlation might imply that summer precipitation events advect heat, thereby promoting melting. On the contrary, annual precipitation is negatively correlated for all regions except for Roi Baudouin West and East, where it shows a positive correlation. If snow that falls during winter is preserved, it builds a protective layer on the surface, contributing to lower albedo and increased snow/firn pore space, slowing the onset of ponding in the following summer (Kuipers Munneke and others, 2014). The different behavior of Roi Baudouin West and East points toward other processes that alter the local dynamics of precipitation and deposition, likely wind. We would expect the same for Roi Baudouin Center as well; however, the trivial correlation ($r = -0.05$) may be a reflection of varied spatial distribution of snow accumulation within the larger Roi Baudouin Ice Shelf. In Dronning Maud Land, average wind speeds are highest around Roi Baudouin (Fig. 7b; >10 m s^{-1} during summer and >15 m s^{-1} annually), which leads to surface scouring and drifting of the precipitated snow throughout the year (Lenaerts and van den Broeke, 2012; Das and others, 2013), exposing blue ice areas having substantially lower albedo (~0.57). As large areas in this region are exposed at lower albedo, melt onset is earlier and melt intensity is higher in general (Johnson and others, 2022).

5.2.3. Energy fluxes

The importance of radiative fluxes in meltwater production have been highlighted for Antarctic Peninsula ice shelves (Luckman and others, 2014; Dirscherl and others, 2021; Laffin and others, 2021) and for East Antarctic ice shelves (Arthur and others, 2022; Dirscherl and others, 2021). Strong shortwave radiation from the sun during summer can lead to a positive near-surface energy budget, heating snow or ice toward the melting point when meltwater can be generated. This can be further intensified in areas with low albedo such as blue ice, frozen lake surfaces, and previously melt-affected snow, promoting the melt-albedo feedback mechanism (e.g. Jakobs and others, 2019). Likewise, incoming longwave radiation can also contribute to a positive energy budget with near-surface warming and/or melting. MAR indicates a relatively stable radiative budget from year to year and from region to region, with 76–81% of the incoming shortwave radiation being reflected as outgoing shortwave radiation, and most

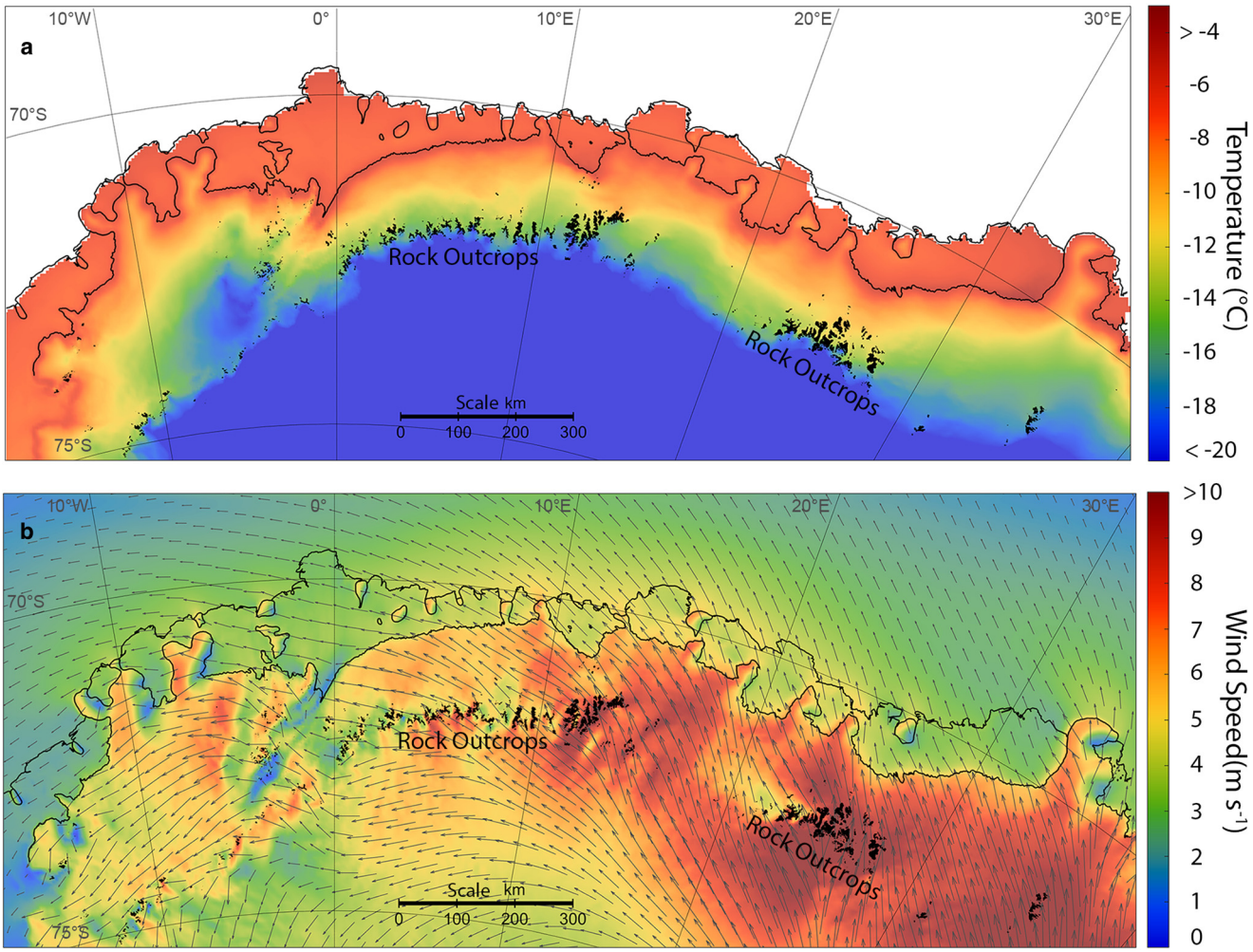

Figure 7. Average summer temperature (a), wind speed and wind direction (b) over Dronning Maud Land estimated using MAR outputs. Black lines representing Antarctic outlines are sourced from SCAR's ADD and outlines of rock outcrops from Burton-Johnson and others (2016) through Quantarctica (Matsuoka and others, 2021).

https://doi.org/10.1017/jog.2024.66 Published online by Cambridge University Press

of the gained energy being balanced by a net energy loss from longwave radiation (Fig. S13). Despite this apparent stability, there are opposing patterns of negative correlations between incoming shortwave radiation and lake extents (five of seven regions, Fig. S11) and positive correlations between longwave incoming radiation and lake extents (six of seven regions, Fig. S11), suggesting that relatively cloudy summers are associated with more melting and ponding (Kittel and others, 2022) than summers with clearer weather. Considering net radiative fluxes, net shortwave radiation appears most important in the west (Riiser Larsen and Fimbulisen, $r = 0.58$–0.84) mainly through reduced outgoing shortwave radiation, likely relating to the melt-albedo feedback (Jakobs and others, 2019). However, net longwave radiation dominates in the east (from Nivlisen to Roi Baudoin Center, $r = 0.40$–0.71). Roi Baudoin East is an exception to this pattern and shows no clear connections with any of the radiative fluxes. The turbulent energy fluxes of sensible and latent heat are highest in the central and eastern regions of Dronning Maud Land where wind speeds are higher (Fig. 7b). The net turbulent flux is slightly positive for all regions, with generally opposite negative and positive correlations with lake extents for the sensible and latent parts, respectively (Fig. 5). Positive correlations with the latent heat flux (i.e. a less negative flux) indicate that rates of evaporation and/or sublimation are lower during years with larger lake extents, reducing the energy loss from the surface. Negative correlations with the sensible heat flux are counter-intuitive, but could be because other positively correlated energy fluxes (latent heat, longwave incoming, shortwave outgoing) are dominant in influencing lake extent dynamics during the melt season. It may also indicate that melting and subsequent ponding in the area is largely driven by radiation at relatively low air temperatures (Jakobs and others, 2020). Summing up all surface energy fluxes into the net energy available for heating and melting, we see a clear positive correlation, giving confidence that MAR can simulate surface melting in a reasonable way. However, in the case of Roi Baudouin East, surface dynamics are highly complex (likely due to fast and persistent winds), leading to a different behavior in comparison to its western counterparts in Dronning Maud Land.

5.2.4. Winds

On a regional scale, near-surface wind speeds are highest around Roi Baudouin, whereas on the western side of Dronning Maud Land winds are generally slower (Fig. 7b), both annually and during summer. Winds can have a direct influence on turbulent heat exchange between surface and atmosphere, but also an indirect one, by scouring or eroding the snow surface leading to reduced albedo and associated increase in absorption of shortwave radiation. An example of the strong relationship between wind speeds and near-surface temperature is shown for Roi Baudouin East in Figure S12. Considering this, the observed negative correlations between lake extents and both wind speed and sensible heat flux for most regions is surprising. One possible explanation is that the highest wind speeds cause drifting snow that reduces energy fluxes at the surface (e.g. Le Toumelin and others, 2021). Directional assessments of wind can reveal the role of downslope wind events, such as föhn and katabatic winds. While no föhn events were identified over eastern Dronning Maud Land, the strong positive correlation with föhn days for Riiser Larsen ($r = 0.73$) and Nivlisen ($r = 0.63$) highlights their role in promoting melting by raising temperatures locally due to warm and dry leeward föhn winds. These föhn winds are caused by the adjacent ice promontories Norvegiaryggen and Søråsen (both for Riiser Larsen) and Leningradkollen (for Nivlisen) that act as topographic barriers to easterly circumpolar winds. The intensity of the föhn induced heating might be due to the heights of the topographic barriers, which in these cases are 706, 668 and 110 m, respectively. The positive correlation with wind speeds during föhn events indicates that stronger föhn events (with higher wind speeds) yield larger melt intensities. Katabatic winds are most prominent over Roi Baudouin, and katabatic days show a strong positive correlation ($r = 0.65$–0.81) with lake extents for all three regions of the ice shelf, in line with the findings of Lenaerts and others (2017). The positive correlation with wind speeds during katabatic events signifies stronger katabatic winds cause more ponding, potentially because fast-flowing katabatic winds generally have a higher warming potential due to the faster rate of adiabatic compression and enhanced vertical mixing of air (Vihma and others, 2011). Further west, katabatic winds are weaker (Fig. S13), whereas in the case of Riser Larsen, the criteria for katabatic days were never fulfilled. The trivial correlation with katabatic days observed for Fimbulisen and Muninisen indicates that katabatics are not vital drivers in these regions as they are relatively weak ($\sim$4–5 m s^{-1}) due obstruction by the upslope nunataks (Fig. 7).

5.2.5. Climate indices

SAM and DMI are representations of larger atmospheric and oceanic teleconnections which may influence surface melting and lake extents. Over the last 50 years SAM has shifted more toward a positive phase (Thompson and Solomon, 2002; Marshall, 2003; Fogt and Marshall, 2020), characterized by thermal isolation and cooling of East Antarctica due to reduced meridional flow of westerlies (van den Broeke and van Lipzig, 2004). During negative SAM periods, more thermal exchange occurs from mid-to-high latitudes of the Southern Hemisphere, leading to an increased katabatic flow (Marshall and others, 2013), coastal easterlies and advection of relatively warm maritime air into East Antarctica (e.g. Orr and others, 2023), thereby warming the East Antarctic continent. These factors could explain the observed negative correlation with SAM for all lake regions ($r = -0.34$ to -0.97; average $r = -0.66$), meaning more melting and larger lake extents during summers with negative SAM. The particularly high-ponding extents observed in 2016/17 and 2019/20 coincide with two negative SAM years, whereas the low-ponding extents observed in 2015/16 and 2020/21 occurred during positive SAM summers (highlighted in Fig. 8). This is corroborated by the negative correlation between continental summer temperature (ERA5) and SAM at $r = -0.56$ ($n = 32$ years), highlighting the role of large-scale atmospheric circulation in driving temperature (and therefore lake variability) in Dronning Maud Land. This negative relationship is also consistent for annual temperature and SAM ($r = -0.61$), and for summer lake extents with respect to annual SAM ($r = -0.35$ to -0.65; average $r = -0.42$). Weak negative correlation between lake extent and DMI suggests that the Indian Ocean Dipole may also play a role in driving lake variability, but to a lesser extent than SAM, further reflected through the weak correlation ($r = 0.19$) between continental summer temperature and DMI.

5.3. Future implications

We have observed significant spatiotemporal lake variability in Dronning Maud Land, driven by a range of climatic factors, highlighting the sensitivity of ice shelves to future melting and subsequent ponding. The lake regions of Fimbulisen and Muninisen that feature only smaller water ponds are exposed to more or less similar climatic conditions (Fig. S13) as their neighboring regions with larger lakes. These two regions may be close to climatic thresholds with a potential for increased ponding in the future.

However, since SAM (both summer and annual) has exhibited a positive trend over last five decades (Thompson and Solomon,

https://doi.org/10.1017/jog.2024.66 Published online by Cambridge University Press

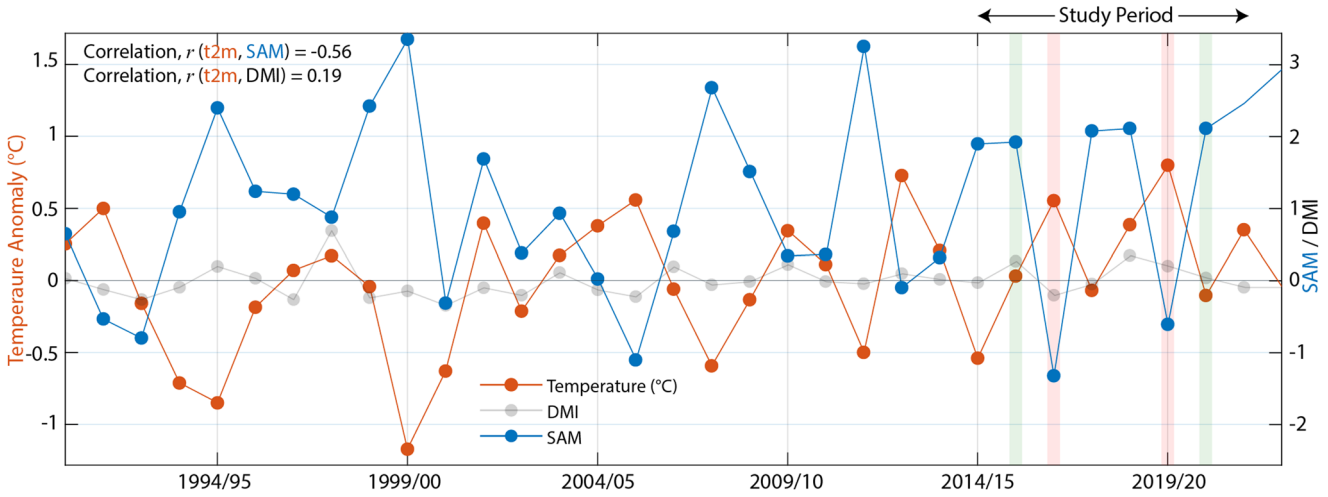

Figure 8. Average surface temperature anomaly (continent wide; left axis) and climate indices SAM and DMI (right axis) over the Southern Hemisphere for summer periods (December–January) during 1990–2022. Red and green shading highlights summers where observations show particularly high and low ponding, respectively, during the study period (2014–21). Correlation between temperature and SAM/DMI is given in the top-left corner.

2002; Marshall, 2003; Fogt and Marshall, 2020) and the most intense ponding in Dronning Maud Land is associated with negative SAM, this could potentially have an opposing effect on future ponding in the area if the trend continues. But the degree to which this would offset the projected temperature rise in future greenhouse gas emission scenarios is uncertain.

Potential growth and expansion of supraglacial lakes can cause the ice shelves to destabilize due to hydrofracture (Lhermitte and others, 2020). Lai and others (2020) assessed the vulnerability of Antarctic ice shelves to hydrofracture using a deep-learning framework with linear elastic fracture mechanics (van der Veen, 1998), and reported that 60 ± 10% of the Antarctic ice shelves with high buttressing potential are currently vulnerable, including Muninisen and parts of Nivlisen in addition to others in Dronning Maud Land (Fig. 4 from Lai and others, 2020). While at present, observed surface meltwater ponding does not coincide much with these hydrofracture-vulnerable areas, it is likely that the expansion of lake extents in future will result in higher risk of hydrofracture. This emphasizes the need for a better understanding of supraglacial lake evolution and potential growth, especially over vulnerable areas that buttress the ice sheet with implications for future predictions of ice-sheet mass balance.

6. Conclusions

Using Landsat 8 and Sentinel-2 archives between 2014 and 2021, we present a multiyear record of supraglacial lake evolution across the entire coastal Dronning Maud Land. We identify seven distinct lake regions situated on five ice shelves and address their evolution patterns from a seasonal to interannual scale. Onset of meltwater ponding occurs between mid-November and early December, mostly upstream of the grounding zones in small topographic depressions. Lake extents peak during mid-to-late January, after which lakes begin to freeze. Riiser Larsen, Nivlisen and Roi Baudouin ice shelves have well-developed networks of lakes and streams that reoccur year after year and transport substantial amounts of meltwater onto the ice shelves, whereas Fimbulisen and Muninisen have smaller networks with little meltwater transfer. In most years during the 2014 to 2021 study period, the magnitude of surface ponding, high or low, is broadly consistent across all the ice shelf regions.

Correlation analysis between seasonal lake extents and high-resolution outputs from the regional climate model MAR shows that relationships between climate and supraglacial lakes are complex, influenced by various factors at different scales. While summer temperatures play a significant role in ponding across all regions, the drivers of temperature variability differ. Factors such as downslope katabatic or föhn winds impact regions differently due to surface topography. Correlations between lake extents and shortwave and longwave radiation suggest that the latter provides more surplus energy for surface melting and ponding. Energy advected by summer rainfall or snowfall contributes further to this process. Winter precipitation adds a snow layer to the surface that acts like a buffer by raising albedo and creating more pore space for retention of meltwater, effectively delaying melt onset and ponding. Downslope katabatic winds contribute locally to increase surface temperature and to expose blue ice areas by snow erosion, promoting a wind-driven albedo feedback on melt, most prominent over the Roi Baudouin Ice Shelf. Föhn winds appear to promote melting and ponding on Riiser Larsen and Nivlisen ice shelves due to local warming on the leeside of ice-sheet promontories. At a region-wide scale, ponding is highest during summers with negative SAM, as observed in 2016/17 and 2019/20. This highlights the role of large-scale atmospheric teleconnections in driving the variability of surface ponding in the region.

Supplementary material. The supplementary material for this article can be found at https://doi.org/10.1017/jog.2024.66.

Data. The MATLAB scripts for mapping lake extents and estimating lake depths using Landsat 8 and Sentinel-2 products are published via GitHub (accessible from https://github.com/anirudhavm/SGL-Mapping-L8-S2). All supraglacial lake products generated from the satellite imagery are published at the Norwegian Polar Data Centre (https://doi.org/10.21334/npolar.2023.31aae21f). Raw imagery of Landsat 8 and Sentinel-2 is available from USGS Earth Explorer Repository (https://earthexplorer.usgs.gov/) and Copernicus Open Access Hub Portal (https://scihub.copernicus.eu/). ERA5 climate reanalysis data can be accessed from the Copernicus Climate Change Service (C3S) Climate Data Store (CDS) Portal (https://cds.climate.copernicus.eu/cdsapp#!/dataset/reanalysis-era5-single-levels; Copernicus Climate Change Service (C3S), 2017). REMA DEM can be downloaded through the Polar Geospatial Center (https://www.pgc.umn.edu/data/rema/). The MAR simulation is available through ftp file services at ftp.climato.be/climato/qglaude/DML_5km/. Monthly SAM and DMI data are available from https://legacy.bas.ac.uk/met/gjma/sam.html and https://psl.noaa.gov/gcos_wgsp/Timeseries/Data/dmi.had.long.data, respectively.

Acknowledgments. This work is a part of the PhD fellowship that A.M. received from the Ministry of Earth Sciences, Government of India through the National Center for Polar and Ocean Research. The authors acknowledge

and appreciate the open data policies of USGS and European Space Agency, from which the Landsat 8 and Sentinel-2 datasets were procured. The authors acknowledge the Polar Geospatial Center (PGC) for generating Reference Elevation Model of Antarctica (REMA) products and making them freely available. Computational resources for the MAR simulations have been provided by the Consortium des Équipements de Calcul Intensif (CÉCI), funded by the Fonds de la Recherche Scientifique de Belgique (F.R.S.-FNRS) under grant No. 2.5020.11 and by the Walloon Region. The authors thank colleagues at Norwegian Polar Institute, University of Oslo and National Center for Polar and Ocean Research for constructive discussions and suggestions for the manuscript.

Author contributions. A.M. and G.M. conceived of and designed the study. Q.G. generated the MAR data used in the study. A.M. carried out the analysis under the guidance of G.M. and T.V.S. A.M. prepared the manuscript. G.M., Q.G. and T.V.S. reviewed and helped improve the manuscript.

References

Agosta C and 10 others (2019) Estimation of the Antarctic surface mass balance using the regional climate model MAR (1979–2015) and identification of dominant processes. *The Cryosphere* **13**(1), 281–296. doi: 10.5194/tc-13-281-2019

Arthur JF, Stokes CR, Jamieson SSR, Carr JR and Leeson A (2020) Distribution and seasonal evolution of supraglacial lakes on Shackleton Ice Shelf, East Antarctica. *The Cryosphere* **14**(11), 4103–4120. doi: 10.5194/tc-14-4103-2020

Arthur JF and 5 others (2022) Large interannual variability in supraglacial lakes around East Antarctica. *Nature Communications* **13**(1), 1711. doi: 10.1038/s41467-022-29385-3

Banwell AF and MacAyeal DR (2015) Ice-shelf fracture due to viscoelastic flexure stress induced by fill/drain cycles of supraglacial lakes. *Antarctic Science* **27**(6), 587–597. doi: 10.1017/S0954102015000292

Banwell AF, MacAyeal DR and Sergienko OV (2013) Breakup of the Larsen B Ice Shelf triggered by chain reaction drainage of supraglacial lakes. *Geophysical Research Letters* **40**(22), 5872–5876. doi: 10.1002/2013GL057694

Banwell AF, Willis IC, Macdonald GJ, Goodsell B and MacAyeal DR (2019) Direct measurements of ice-shelf flexure caused by surface meltwater ponding and drainage. *Nature Communications* **10**(1), 1–10. doi: 10.1038/s41467-019-08522-5

Banwell AF and 7 others (2021) The 32-year record-high surface melt in 2019/2020 on the northern George VI ice shelf, Antarctic Peninsula. *The Cryosphere* **15**(2), 909–925. doi: 10.5194/tc-15-909-2021

Banwell AF, Willis IC, Stevens LA, Dell RL and MacAyeal DR (2024) Observed meltwater-induced flexure and fracture at a doline on George VI Ice Shelf, Antarctica. *Journal of Glaciology*, 1–14. doi: 10.1017/jog.2024.31

Bell RE, Banwell AF, Trusel LD and Kingslake J (2018) Antarctic surface hydrology and impacts on ice-sheet mass balance. *Nature Climate Change* **8**(12), 1044–1052. doi: 10.1038/s41558-018-0326-3

Brandt RE and Warren SG (1993) Solar-heating rates and temperature profiles in Antarctic snow and ice. *Journal of Glaciology* **39**(131), 99–110. doi: 10.3189/S0022143000015756

Brun E, David P, Sudul M and Brunot G (1992) A numerical model to simulate snow-cover stratigraphy for operational avalanche forecasting. *Journal of Glaciology* **38**(128), 13–22. doi: 10.3189/S0022143000009552

Burton-Johnson A, Black M, Peter TF and Kaluza-Gilbert J (2016) An automated methodology for differentiating rock from snow, clouds and sea in Antarctica from Landsat 8 imagery: a new rock outcrop map and area estimation for the entire Antarctic continent. *Cryosphere* **10**(4), 1665–1677. doi: 10.5194/tc-10-1665-2016

Buth LG and 5 others (2022) Sentinel-1 detection of seasonal and perennial firn aquifers in the Antarctic Peninsula. *The Cryosphere Discussion* **20**(October), 1–20. doi: 10.5194/tc-2022-127

Cape MR and 5 others (2015) Foehn winds link climate-driven warming to ice shelf evolution in Antarctica. *Journal of Geophysical Research: Atmospheres* **120**(21), 11,037–11,057. doi: 10.1002/2015JD023465

Copernicus Climate Change Service (C3S) (2017) ERA5: fifth generation of ECMWF atmospheric reanalyses of the global climate. Copernicus Climate Change Service Climate Data Store.

Das I and 9 others (2013) Influence of persistent wind scour on the surface mass balance of Antarctica. *Nature Geoscience* **6**(5), 367–371. doi: 10.1038/ngeo1766

Datta RT and 5 others (2018) melting over the northeast Antarctic Peninsula (1999–2009): evaluation of a high-resolution regional climate model. *The Cryosphere* **12**(9), 2901–2922. doi: 10.5194/tc-12-2901-2018

Datta RT and 6 others (2019) The effect of foehn-induced surface melt on firn evolution over the northeast Antarctic Peninsula. *Geophysical Research Letters* **46**(7), 3822–3831. doi: 10.1029/2018GL080845

Davis AMJ and Mcnider RT (1997) The development of Antarctic katabatic winds and implications for the coastal ocean. *Journal of the Atmospheric Sciences* **54**(9), 1248–1261. doi: 10.1175/1520-0469(1997)054<1248:TDOAKW>2.0.CO;2

Dee DP and 35 others (2011) The ERA-Interim reanalysis: configuration and performance of the data assimilation system. *Quarterly Journal of the Royal Meteorological Society* **137**(656), 553–597. doi: 10.1002/qj.828

Dell R and 6 others (2020) Lateral meltwater transfer across an Antarctic Ice Shelf. *The Cryosphere* **14**(7), 2313–2330. doi: 10.5194/tc-14-2313-2020

Dell R and 6 others (2022) Supervised classification of slush and ponded water on Antarctic ice shelves using Landsat 8 imagery. *Journal of Glaciology* **68**(268), 401–414. doi: 10.1017/jog.2021.114

Dell RL, Willis IC, Arnold NS, Banwell AF and de Roda Husman S (2024) Substantial contribution of slush to meltwater area across Antarctic ice shelves. *Nature Geoscience* **17**(7), 624–630. doi: 10.1038/s41561-024-01466-6

De Ridder K and Gallée H (1998) Land surface-induced regional climate change in southern Israel. *Journal of Applied Meteorology* **37**(11), 1470–1485. doi: 10.1175/1520-0450(1998)037<1470:LSIRCC>2.0.CO;2

Dirscherl MC, Dietz AJ and Kuenzer C (2021) Seasonal evolution of Antarctic supraglacial lakes in 2015–2021 and links to environmental controls. *The Cryosphere* **15**(11), 5205–5226. doi: 10.5194/tc-15-5205-2021

Dunmire D and 11 others (2020) Observations of buried lake drainage on the Antarctic Ice Sheet. *Geophysical Research Letters* **47**(15), 1–9. doi: 10.1029/2020GL087970

Dupont TK and Alley RB (2005) Assessment of the importance of ice-shelf buttressing to ice-sheet flow. *Geophysical Research Letters* **32**(4), 1–4. doi: 10.1029/2004GL022024

Fogt RL and Marshall GJ (2020) The southern annular mode: variability, trends, and climate impacts across the Southern Hemisphere. *WIREs Climate Change* **11**(4), 1–24. doi: 10.1002/wcc.652

Fretwell P and 59 others (2013) Bedmap2: improved ice bed, surface and thickness datasets for Antarctica. *The Cryosphere* **7**(1), 375–393. doi: 10.5194/tc-7-375-2013

Fürst JJ and 6 others (2016) The safety band of Antarctic ice shelves. *Nature Climate Change* **6**(5), 479–482. doi: 10.1038/nclimate2912

Gagliardini O, Durand G, Zwinger T, Hindmarsh RCA and Le Meur E (2010) Coupling of ice-shelf melting and buttressing is a key process in ice-sheets dynamics. *Geophysical Research Letters* **37**(14), 1–5. doi: 10.1029/2010GL043334

Gallée H (1995) Simulation of the mesocyclonic activity in the Ross Sea, Antarctica. *Monthly Weather Review* **123**(7), 2051–2069. doi: 10.1175/1520-0493(1995)123<2051:SOTMAI>2.0.CO;2

Gallée H and Schayes G (1994) Development of a three-dimensional meso-γ primitive equation model: katabatic winds simulation in the area of Terra Nova Bay, Antarctica. *Monthly Weather Review* **122**(4), 671–685. doi: 10.1175/1520-0493(1994)122<0671:DOATDM>2.0.CO;2

Gilbert E and Kittel C (2021) Surface melt and runoff on Antarctic ice shelves at 1.5°C, 2°C, and 4°C of future warming. *Geophysical Research Letters* **48**(8), 1–9. doi: 10.1029/2020GL091733

Glasser NF and 5 others (2011) From ice-shelf tributary to tidewater glacier: continued rapid recession, acceleration and thinning of Röhss Glacier following the 1995 collapse of the Prince Gustav Ice Shelf, Antarctic Peninsula. *Journal of Glaciology* **57**(203), 397–406. doi: 10.3189/002214311796905578

Glaude Q and 6 others (2020) Empirical removal of tides and inverse barometer effect on DInSAR from double DInSAR and a regional climate model. *IEEE Journal of Selected Topics in Applied Earth Observations and Remote Sensing* **13**, 4085–4094. doi: 10.1109/JSTARS.2020.3008497

Goel V and 5 others (2020) Characteristics of ice rises and ice rumples in Dronning Maud Land and Enderby Land, Antarctica. *Journal of Glaciology* **66**(260), 1064–1078. doi: 10.1017/jog.2020.77

Hersbach H and 42 others (2020) The ERA5 global reanalysis. *Quarterly Journal of the Royal Meteorological Society* **146**(730), 1999–2049. doi: 10.1002/qj.3803

Hofer S and 5 others (2021) The contribution of drifting snow to cloud properties and the atmospheric radiative budget over Antarctica. *Geophysical Research Letters* **48**(22), 1–11. doi: 10.1029/2021GL094967

Howat IM, Porter C, Smith BE, Noh M-J and Morin P (2019) The reference elevation model of Antarctica. *The Cryosphere* **13**(2), 665–674. doi: 10.5194/tc-13-665-2019

Hubbard B and 12 others (2016) Massive subsurface ice formed by refreezing of ice-shelf melt ponds. *Nature Communications* **7**(May), 1–6. doi: 10.1038/ncomms11897

Hui F and 12 others (2014) Mapping blue-ice areas in Antarctica using ETM+ and MODIS data. *Annals of Glaciology* **55**(66), 129–137. doi: 10.3189/2014AoG66A069

Jakobs CL, Reijmer CH, Kuipers Munneke P, König-Langlo G and Van Den Broeke MR (2019) Quantifying the snowmelt-albedo feedback at Neumayer Station, East Antarctica. *The Cryosphere* **13**(5), 1473–1485. doi: 10.5194/tc-13-1473-2019

Jakobs CL and 6 others (2020) A benchmark dataset of in situ Antarctic surface melt rates and energy balance. *Journal of Glaciology* **66**(256), 291–302. doi: 10.1017/jog.2020.6

Johnson A, Hock R and Fahnestock M (2022) Spatial variability and regional trends of Antarctic ice shelf surface melt duration over 1979–2020 derived from passive microwave data. *Journal of Glaciology* **68**(269), 533–546. doi: 10.1017/jog.2021.112

Kingslake J, Ng F and Sole A (2015) Modelling channelized surface drainage of supraglacial lakes. *Journal of Glaciology* **61**(225), 185–199. doi: 10.3189/2015JoG14J158

Kingslake J, Ely JC, Das I and Bell RE (2017) Widespread movement of meltwater onto and across Antarctic ice shelves. *Nature* **544**(7650), 349–352. doi: 10.1038/nature22049

Kittel C and 10 others (2021) Diverging future surface mass balance between the Antarctic ice shelves and grounded ice sheet. *The Cryosphere* **15**(3), 1215–1236. doi: 10.5194/tc-15-1215-2021

Kittel C and 9 others (2022) Clouds drive differences in future surface melt over the Antarctic ice shelves. *The Cryosphere* **16**(7), 2655–2669. doi: 10.5194/tc-16-2655-2022

Kuipers Munneke P, Ligtenberg SRM, van den Broeke MR, van Angelen JH and Forster RR (2014) Explaining the presence of perennial liquid water bodies in the firn of the Greenland Ice Sheet. *Geophysical Research Letters* **41**(2), 476–483. doi: 10.1002/2013GL058389

Laffin MK and 5 others (2021) Climatology and evolution of the Antarctic Peninsula föhn wind-induced melt regime from 1979–2018. *Journal of Geophysical Research: Atmospheres* **126**(4), 1–19. doi: 10.1029/2020JD033682

Lai CY and 7 others (2020) Vulnerability of Antarctica's ice shelves to meltwater-driven fracture. *Nature* **584**(7822), 574–578. doi: 10.1038/s41586-020-2627-8

Lambin C, Fettweis X, Kittel C, Fonder M and Ernst D (2023) Assessment of future wind speed and wind power changes over South Greenland using the Modèle Atmosphérique Régional regional climate model. *International Journal of Climatology* **43**(1), 558–574. doi: 10.1002/joc.7795

Langley ES, Leeson A, Stokes CR and Jamieson SSR (2016) Seasonal evolution of supraglacial lakes on an east Antarctic outlet glacier. *Geophysical Research Letters* **43**(16), 8563–8571. doi: 10.1002/2016GL069511

Leeson A, Forster E, Rice A, Gourmelen N and Wessem JM (2020) Evolution of supraglacial lakes on the Larsen B Ice Shelf in the decades before it collapsed. *Geophysical Research Letters* **47**(4), 1–9. doi: 10.1029/2019GL085591

Lenaerts JTM and van den Broeke MR (2012) Modeling drifting snow in Antarctica with a regional climate model: 2. Results. *Journal of Geophysical Research: Atmospheres* **117**(D5), 1–11. doi: 10.1029/2010JD015419

Lenaerts JTM and 12 others (2017) Meltwater produced by wind–albedo interaction stored in an east Antarctic ice shelf. *Nature Climate Change* **7**(1), 58–62. doi: 10.1038/nclimate3180

Le Toumelin L and 7 others (2021) Sensitivity of the surface energy budget to drifting snow as simulated by MAR in coastal Adelie Land, Antarctica. *The Cryosphere* **15**(8), 3595–3614. doi: 10.5194/tc-15-3595-2021

Lhermitte S and 7 others (2020) Damage accelerates ice shelf instability and mass loss in Amundsen Sea Embayment. *Proceedings of the National Academy of Sciences* **117**(40), 24735–24741. doi: 10.1073/pnas.1912890117

Liang YL and 7 others (2012) A decadal investigation of supraglacial lakes in West Greenland using a fully automatic detection and tracking algorithm. *Remote Sensing of Environment* **123**, 127–138. doi: 10.1016/j.rse.2012.03.020

Liston GE, Bruland O, Winther J-G, Elvehøy H and Sand K (1999) Meltwater production in Antarctic blue-ice areas: sensitivity to changes in atmospheric forcing. *Polar Research* **18**(2), 283–290. doi: 10.3402/polar.v18i2.6586

Luckman A and 6 others (2014) Surface melt and ponding on Larsen C Ice Shelf and the impact of föhn winds. *Antarctic Science* **26**(6), 625–635. doi: 10.1017/S0954102014000339

Marshall GJ (2003) Trends in the southern annular mode from observations and reanalyses. *Journal of Climate* **16**(24), 4134–4143. doi: 10.1175/1520-0442(2003)016<4134:TITSAM>2.0.CO;2

Marshall GJ, Orr A and Turner J (2013) A predominant reversal in the relationship between the SAM and east Antarctic temperatures during the twenty-first century. *Journal of Climate* **26**(14), 5196–5204. doi: 10.1175/JCLI-D-12-00671.1

Matsuoka K and 21 others (2021) Quantarctica, an integrated mapping environment for Antarctica, the Southern Ocean, and sub-Antarctic islands. *Environmental Modelling & Software* **140**, 105015. doi: 10.1016/j.envsoft.2021.105015

Morcrette J-J (2002) Assessment of the ECMWF model cloudiness and surface radiation fields at the ARM SGP site. *Monthly Weather Review* **130**(2), 257–277. doi: 10.1175/1520-0493(2002)130<0257:AOTEMC>2.0.CO;2

Mottram R and 16 others (2021) What is the surface mass balance of Antarctica? An intercomparison of regional climate model estimates. *The Cryosphere* **15**(8), 3751–3784. doi: 10.5194/tc-15-3751-2021

Moussavi M and 5 others (2020) Antarctic supraglacial lake detection using Landsat 8 and Sentinel-2 imagery: towards continental generation of lake volumes. *Remote Sensing* **12**(1), 134. doi: 10.3390/rs12010134

Muñoz-Sabater J and 16 others (2021) ERA5-Land: a state-of-the-art global reanalysis dataset for land applications. *Earth System Science Data* **13**(9), 4349–4383. doi: 10.5194/essd-13-4349-2021

Orr A and 17 others (2023) Characteristics of surface 'melt potential' over Antarctic ice shelves based on regional atmospheric model simulations of summer air temperature extremes from 1979/80 to 2018/19. *Journal of Climate* **36**(10), 3357–3383. doi: 10.1175/JCLI-D-22-0386.1

Parish TR and Bromwich DH (1987) The surface windfield over the Antarctic ice sheets. *Nature* **328**(6125), 51–54. doi: 10.1038/328051a0

Phartiyal B, Sharma A and Bera SK (2011) Glacial lakes and geomorphological evolution of Schirmacher Oasis, East Antarctica, during Late Quaternary. *Quaternary International* **235**(1–2), 128–136. doi: 10.1016/j.quaint.2010.11.025

Picard G, Fily M and Gallee H (2007) Surface melting derived from microwave radiometers: a climatic indicator in Antarctica. *Annals of Glaciology* **46**(2002), 29–34. doi: 10.3189/172756407782871684

Pope A and 6 others (2016) Estimating supraglacial lake depth in West Greenland using Landsat 8 and comparison with other multispectral methods. *The Cryosphere* **10**(1), 15–27. doi: 10.5194/tc-10-15-2016

Pritchard HD, Arthern RJ, Vaughan DG and Edwards LA (2009) Extensive dynamic thinning on the margins of the Greenland and Antarctic ice sheets. *Nature* **461**(7266), 971–975. doi: 10.1038/nature08471

Rignot E (2004) Accelerated ice discharge from the Antarctic Peninsula following the collapse of Larsen B Ice Shelf. *Geophysical Research Letters* **31**(18), L18401. doi: 10.1029/2004GL020697

Rignot E, Jacobs S, Mouginot J and Scheuchl B (2013) Ice-shelf melting around Antarctica. *Science* **341**(6143), 266–270. doi: 10.1126/science.1235798

Rott H, Skvarca P and Nagler T (1996) Rapid collapse of northern Larsen Ice Shelf, Antarctica. *Science* **271**(5250), 788–792. doi: 10.1126/science.271.5250.788

Saunderson D, Mackintosh A, McCormack F, Jones RS and Picard G (2022) Surface melt on the Shackleton Ice Shelf, East Antarctica (2003–2021). *The Cryosphere* **16**(10), 4553–4569. doi: 10.5194/tc-16-4553-2022

Scambos TA, Hulbe C, Fahnestock M and Bohlander J (2000) The link between climate warming and break-up of ice shelves in the Antarctic Peninsula. *Journal of Glaciology* **46**(154), 516–530. doi: 10.3189/172756500781833043

Scambos TA and 7 others (2009) Ice shelf disintegration by plate bending and hydro-fracture: satellite observations and model results of the 2008 Wilkins ice shelf break-ups. *Earth and Planetary Science Letters* **280**(1–4), 51–60. doi: 10.1016/j.epsl.2008.12.027

Schlatter TW (1972) The local surface energy balance and subsurface temperature regime in Antarctica. *Journal of Applied Meteorology* **11**(7), 1048–1062. doi: 10.1175/1520-0450(1972)011<1048:TLSEBA>2.0.CO;2

Spergel JJ, Kingslake J, Creyts T, van Wessem M and Fricker HA (2021) Surface meltwater drainage and ponding on Amery Ice Shelf, East

Antarctica, 1973–2019. *Journal of Glaciology* **67**(266), 985–998. doi: 10.1017/jog.2021.46

Stokes CR, Sanderson JE, Miles BWJ, Jamieson SSR and Leeson A (2019) Widespread distribution of supraglacial lakes around the margin of the East Antarctic Ice Sheet. *Scientific Reports* **9**(1), 1–14. doi: 10.1038/s41598-019-50343-5

Tedesco M and 5 others (2016) The darkening of the Greenland Ice Sheet: trends, drivers, and projections (1981–2100). *The Cryosphere* **10**(2), 477–496. doi: 10.5194/tc-10-477-2016

Thompson DWJ and Solomon S (2002) Interpretation of recent Southern Hemisphere climate change. *Science* **296**(5569), 895–899. doi: 10.1126/science.1069270

Trusel LD, Frey KE and Das SB (2012) Antarctic surface melting dynamics: enhanced perspectives from radar scatterometer data. *Journal of Geophysical Research: Earth Surface* **117**(2), 1–15. doi: 10.1029/2011JF002126

Trusel LD, Frey KE, Das SB, Munneke PK and Van Den Broeke MR (2013) Satellite-based estimates of Antarctic surface meltwater fluxes. *Geophysical Research Letters* **40**(23), 6148–6153. doi: 10.1002/2013GL058138

Tuckett PA and 6 others (2019) Rapid accelerations of Antarctic Peninsula outlet glaciers driven by surface melt. *Nature Communications* **10**(1), 1–8. doi: 10.1038/s41467-019-12039-2

Tuckett PA and 6 others (2021) Automated mapping of the seasonal evolution of surface meltwater and its links to climate on the Amery Ice Shelf, Antarctica. *The Cryosphere* **15**(12), 5785–5804. doi: 10.5194/tc-15-5785-2021

van den Broeke MR and van Lipzig NPM (2004) Changes in Antarctic temperature, wind and precipitation in response to the Antarctic Oscillation. *Annals of Glaciology* **39**, 119–126. doi: 10.3189/172756404781814654

van der Veen C (1998) Fracture mechanics approach to penetration of bottom crevasses on glaciers. *Cold Regions Science and Technology* **27**(3), 213–223. doi: 10.1016/S0165-232X(98)00006-8

van Wessem JM and 18 others (2018) Modelling the climate and surface mass balance of polar ice sheets using RACMO2 – part 2: Antarctica (1979–2016). *The Cryosphere* **12**(4), 1479–1498. doi: 10.5194/tc-12-1479-2018

Vihma T, Tuovinen E and Savijärvi H (2011) Interaction of katabatic winds and near-surface temperatures in the Antarctic. *Journal of Geophysical Research: Atmospheres* **116**(D21), 1–14. doi: 10.1029/2010JD014917

Warner RC and 5 others (2021) Rapid formation of an ice doline on Amery Ice Shelf, East Antarctica. *Geophysical Research Letters* **48**(14), 1–11. doi: 10.1029/2020GL091095

Winther JG, Elvehøy H, Bøggild CE, Sand K and Liston G (1996) Melting, runoff and the formation of frozen lakes in a mixed snow and blue-ice field in Dronning Maud Land, Antarctica. *Journal of Glaciology* **42**(141), 271–278. doi: 10.1017/S0022143000004135

https://doi.org/10.1017/jog.2024.66 Published online by Cambridge University Press